Journal of Translational Medicine

RESEARCH

Open Access

Single-cell and spatial analyses reveal endothelial–macrophage inflammatory crosstalk in dry age-related macular degeneration

Yujie Chen[1†], Chuling Liu[1†], Jinghan Chen[1†], Yimin Huang[2,3], Guiping Pan[4], Pan Wang[4], Yishan Hu[1], Lin Chen[5*], Yuxi Zhang[6,7*] and Yan Wang[4*]

Abstract

Background Dry age-related macular degeneration (AMD) is characterized by progressive degeneration of the retinal pigment epithelium–choroid interface, accompanied by immune dysregulation. However, the cellular interactions and regulatory mechanisms driving macrophage activation in this process remain incompletely understood.

Methods We integrated spatial transcriptomics and single-cell RNA sequencing data from a photo-oxidative damage mouse model and human dry AMD samples. A series of bioinformatic analyses, including cell–cell communication analysis, enrichment analysis, and pseudotime trajectory analysis, were performed to characterize cellular features and regulatory pathways.

Results In the photo-oxidative damage mouse model, the RPE–choroid region showed marked infiltration of myeloid cells. In human dry AMD samples, SLC16A10-positive macrophages were enriched and exhibited pro-inflammatory features. Further analysis revealed that endothelial cells regulate SLC16A10-positive macrophages through the TNFSF10–TNFRSF10B pathway, with NFKB1 acting as a key regulator to activate NF-κB signaling, thereby promoting the formation of a vascular–immune inflammatory niche.

Conclusions This study systematically characterizes immune remodeling in the RPE–choroid region in dry AMD and identifies an endothelial–macrophage TNFSF10–TNFRSF10B–NF-κB signaling pathway that drives disease progression. These findings provide new insights into disease mechanisms and suggest potential therapeutic targets for dry AMD.

†Yujie Chen, Chuling Liu and Jinghan Chen contributed equally to this work.

*Correspondence:
Lin Chen
2016746832@qq.com
Yuxi Zhang
Yyyuxi15014629273@163.com
Yan Wang
ykwy1976@163.com

Full list of author information is available at the end of the article

Keywords Age-related macular degeneration, Dry AMD, Macrophages, Single-cell RNA sequencing, Spatial transcriptomics, TNFSF10–TNFRSF10B signaling

Background

Age-related macular degeneration (AMD) is a leading cause of irreversible vision loss worldwide, with a rapidly increasing global burden driven by population aging [1–3]. Clinically, AMD progresses from early and intermediate stages to late-stage disease, characterized by central geographic atrophy (GA) or choroidal neovascularization, both of which result in severe visual impairment [4].

GA is defined by progressive degeneration of the retinal pigment epithelium (RPE), photoreceptor loss, and structural disruption of the retina–choroid interface, accompanied by choriocapillaris alterations [5, 6]. Increasing evidence suggests that AMD progression is driven not only by neuroretinal degeneration but also by chronic inflammation within the RPE–choroid niche [7, 8]. This persistent inflammatory state is characterized by sustained activation of immune cells, particularly myeloid cells, which contribute to tissue degeneration through the production of inflammatory mediators [9, 10].

In parallel, the choroidal vasculature plays a critical role in maintaining local tissue homeostasis. Choriocapillaris damage progresses with disease severity and is associated with alterations in the local vascular–immune niche in AMD [11–13]. Endothelial cells actively regulate immune responses by secreting cytokines and chemokines, thereby influencing immune cell recruitment and activation and shaping the vascular–immune niche [14, 15]. However, how endothelial cells regulate macrophage activation and their interactions within the RPE–choroid niche in GA remains poorly understood.

Despite advances in anti-vascular endothelial growth factor therapy for neovascular AMD, effective treatments for dry AMD, particularly at the GA stage, remain limited [16]. This highlights the need to investigate endothelial–immune interactions beyond angiogenesis to identify new therapeutic targets.

In this study, we integrated spatial transcriptomics and single-cell RNA sequencing to characterize macrophage heterogeneity and cell–cell communication in the RPE–choroid niche, with a focus on endothelial–macrophage interactions. We aimed to identify key endothelial-derived signaling pathways that drive macrophage activation and inflammatory remodeling in dry AMD.

Methods

Mouse spatial transcriptomics sequencing and data processing

Upstream analysis

Mouse eye spatial transcriptomics data were downloaded from the Gene Expression Omnibus (GEO; accession: GSE248517), comprising seven samples, including one Control sample (n = 1) and six PD samples (PD1D, PD3D, and PD5D, with n = 2 per time point). These samples were originally reported by Schumann U et al. [17]. (see Supplementary Table 1 for detailed sample information).

All data had been preprocessed using the 10x Genomics Space Ranger pipeline, including filtered gene–barcode matrices (matrix.mtx), gene feature files (features.tsv), and barcode files (barcodes.tsv), and were directly used for downstream analyses.

Downstream analysis

1. Data preprocessing:

Data preprocessing and integration were performed in RStudio using the Seurat (v5.3.1) and Semla (v1.3.1) packages [18, 19]. Raw gene expression matrices were imported using the Read10X function, and Seurat objects were constructed using CreateSeuratObject.Quality control was conducted by excluding spatial spots with fewer than 500 detected genes or with mitochondrial gene content > 30%. After filtering, a total of 3,640 spots were retained, including 577 (Control), 532 (PD1Drep1), 510 (PD1Drep2), 611 (PD3Drep1), 473 (PD3Drep2), 439 (PD5Drep1), and 498 (PD5Drep2).Data were normalized using the NormalizeData function with the "LogNormalize" method and a scale factor of 10,000. Highly variable genes were identified using the FindVariableFeatures function with the variance-stabilizing transformation (vst) method [20], and the top 2,000 features were selected.Integration anchors across the seven datasets were identified using FindIntegrationAnchors based on canonical correlation analysis (CCA), followed by data integration. The integrated data were scaled using ScaleData, and principal component analysis (PCA) was performed using RunPCA (top 10 principal components retained). UMAP was then applied using RunUMAP for dimensionality reduction and visualization [21].A shared nearest neighbor (SNN) graph was constructed using FindNeighbors, and unsupervised clustering was performed using FindClusters with a resolution of 0.8. Cell type annotation was achieved by integrating spatial localization from H&E-stained images with cluster-specific marker genes identified using FindAllMarkers. Visualization of UMAP clustering and spatial gene expression patterns was performed using SCP (v0.5.6) (https://github.com/zhanghao-njmu/SCP) and ggplot2 (v4.0.2) [22]. Spatial visualization of cluster labels and feature expression

was further conducted using the MapLabels and MapFeatures functions in Semla.

(2) Spatial transcriptomics deconvolution:

To characterize the spatial distribution of cell types, the Robust Cell Type Decomposition (RCTD) method implemented in the spacexr R package (v2.2.1) was applied [23]. This method maps cell subtypes defined by single-cell RNA sequencing (scRNA-seq) data onto Visium spatial transcriptomics data and estimates the proportion of each cell type or state within individual spatial spots using a probabilistic framework.

A reference scRNA-seq dataset was constructed from mouse eye tissues, including the bipolar cell layer (BCL), photoreceptor layer (PRL), and retinal pigment epithelium/choroid (RPE/Choroid), comprising three samples (GSM6914767, GSM7677901, and GSM8372459). Given the complex laminar structure of the retina and the relatively low resolution of Visium data, the "full" mode (doublet_mode = "full") was used, allowing each spatial spot to be modeled as a mixture of multiple cell types. This approach improves the accuracy of cell-type mapping in regions of interest. Normalized cell-type abundances (z-scores) were subsequently calculated across spatial regions.

(3) Differential expression and enrichment analysis:

Differential expression analysis was performed using the FindMarkers function in Seurat with the Wilcoxon rank-sum test to identify significantly upregulated genes in the retinal pigment epithelium and choroid (RPE/Choroid) of PD groups compared with the Control group (adjusted $p < 0.05$ and fold change > 1.5).

Gene Ontology (GO) biological process (BP) enrichment analysis was conducted using the enrichGO function in the clusterProfiler package [24]. Only results with an adjusted p value ≤ 0.05 were considered statistically significant.

Mouse single cell transcriptome sequencing and data processing

Data processing using cell ranger

The transcriptomic datasets integrated in this study were obtained from publicly available datasets GSE222094, GSE239941, and GSE271262 (detailed sample information is provided in Supplementary Table 1) [25–27]. All datasets were processed using a standardized pipeline starting from raw FASTQ files to ensure analytical consistency.

Sequencing data were processed using Cell Ranger software (v8.0.1, 10x Genomics). Reads were aligned to the mouse reference genome GRCm39 (Mus musculus; GENCODE vM33 annotation; refdata-gex-GRCm39-2024-A) provided by 10x Genomics. Sequence alignment, UMI counting, and cell barcode identification were performed following the official 10x Genomics recommended pipeline, resulting in gene expression matrices for downstream analysis.

Quality control and clustering analysis

Single-cell RNA-seq data were analyzed and visualized using Seurat, SCP, and other R packages. Quality control criteria were applied to exclude cells with fewer than 500 or more than 6,000 detected genes, mitochondrial gene content > 20%, ribosomal gene content > 20%, or gene complexity scores (log10GenesPerUMI) < 0.8.

Potential doublets were identified and removed using scDblFinder (v1.22.0) [28], resulting in a total of 28,452 high-quality cells retained for downstream analysis.

The filtered data were normalized using the NormalizeData function with log normalization, followed by data scaling using ScaleData to mitigate technical variation. Highly variable genes were identified using the FindVariableFeatures function, and the top 2,000 genes were selected for downstream analysis.

Principal component analysis (PCA) was performed using the RunPCA function, and the top 11 principal components were selected for subsequent dimensionality reduction and clustering. To correct for batch effects arising from different sample sources, Harmony (v1.2.4) was applied using sample identity as the grouping variable [29].

Following Harmony correction, a shared nearest neighbor (SNN) graph was constructed using the FindNeighbors function, and clustering was performed using the FindClusters function with a resolution of 0.8 to identify distinct cell populations.

Human single cell transcriptome sequencing and data processing

Data processing using cell ranger

The transcriptomic datasets integrated in this study were obtained from publicly available datasets GSE210543, GSE188280, GSE230348, and GSE203499 (detailed sample information is provided in Supplementary Table 2) [30, 31]. All data were processed using a standard analysis pipeline, starting from raw FASTQ files, to ensure consistency of results. Sequencing data were processed using Cell Ranger software (v8.0.1, 10x Genomics). The reference genome used was the GRCh38 version (Homo sapiens, GENCODE v44 annotation, refdata-gex-GRCh38-2024-A) provided by 10x Genomics, and sequence alignment, UMI quantification, and cell barcode identification were performed strictly according to the official 10x Genomics recommended pipeline (https://www.10xgenomics.com/support/software/cell-range

r/downloads/cr-ref-build-steps), ultimately generating standardized gene expression matrices for downstream analysis.

Quality control and clustering analysis

Single-cell data were analyzed and visualized using Seurat, SCP, and other R packages. The quality control criteria were as follows: cells with fewer than 500 or more than 6000 detected genes, mitochondrial gene proportion > 20%, ribosomal gene proportion > 20%, or gene complexity score (log10GenesPerUMI) < 0.8 were excluded. Potential doublets were identified and removed using scDblFinder (v1.22.0), and a total of 41,828 high-quality cells were retained for downstream analysis (n_Control = 26,848, n_dAMD = 14,980).

The filtered data were first normalized using the log-normalization method (NormalizeData), and subsequently scaled using ScaleData to correct for potential technical variation. The top 2,000 highly variable genes were selected using the FindVariableFeatures function for downstream analysis. Principal component analysis (PCA) was then performed using RunPCA, and the top 18 principal components were selected for subsequent dimensionality reduction and clustering analysis. To eliminate batch effects caused by different sample sources, Harmony (v1.2.4) was applied, using sample origin as the grouping variable for data integration and batch correction.

In the Harmony-corrected low-dimensional space, a shared nearest neighbor (SNN) graph was constructed using FindNeighbors, and clustering analysis was performed using the FindClusters function (resolution = 0.7), thereby identifying distinct cell populations.

Downstream analysis

1. Differential gene analysis:

DEGs among all cell clusters were analyzed using the FindAllMarkers function in Seurat [32], with the minimum expression proportion (min.pct) set to 0.25, requiring that the gene be expressed in at least 25% of cells in at least one cluster. The Wilcoxon rank-sum test (Wilcox test) was applied, and the adjusted P-value threshold was set to 0.05, while the log2 fold change threshold was set to log2(1.5).

(2) Enrichment analysis:

① Based on the differential expression analysis results, enrichment analysis was performed using the R package clusterProfiler (version 4.16.0) in both the GO Biological Process (GO_BP) and KEGG databases, with a significance threshold of $p < 0.05$.

② Gene set enrichment analysis (GSEA) was also performed using clusterProfiler (version 4.16.0) [33], with a significance threshold of adjusted $p < 0.05$. Visualization of GSEA results was achieved using the gseaplot2 function in the R package enrichplot (version 1.28.4, https://bioconductor.org/packages/enrichplot).

(3) Cell–cell interaction analysis:

Cell–cell communication analysis was performed using CellChat (v2.1.2) [34], scCrossTalk (v1.0) [35], and nichenetr (v2.2.0) [36].

① Based on the Seurat object, a CellChat object was constructed, and cell type information was embedded as metadata. To ensure database consistency, the built-in CellChat database was replaced with the scCrossTalk database for analysis. CellChat calculates the probability value (prob) of overexpressed ligand–receptor pairs in each cell group to quantify the communication strength between different cell groups. In the generated bubble plots, communication strength was displayed after transformation as log10(prob) + 1, with values limited to the range of 0–1.

② At the same time, RNA counts data and cell type information were extracted from the Seurat object, and genes were standardized and annotated using rev_gene. The processed expression matrix and cell type information were used to construct a scCrossTalk object and perform ligand–receptor pair analysis. In this analysis, only ligand–receptor pairs expressed in at least 10 cells and detected in at least 10% of cells were retained, with a significance threshold set at $p < 0.05$. The final extracted cell–cell interaction (CCI) network was used for subsequent analysis.

③ NicheNet analysis focused on the DEGs of SLC16A10^{+} macrophages, from which potential downstream target genes were extracted and used for subsequent analysis to explore signaling pathways and functional effects that may be dominated by macrophages under dAMD conditions.

(4) Single-cell weighted gene co-expression network analysis (WGCNA):

Weighted gene co-expression network analysis was performed using the R package hdWGCNA (v0.4.03) [37, 38]. First, the Seurat object was preprocessed using SetupForWGCNA, and genes expressed in at least 5% of cells (fraction = 0.05) were selected for subsequent analysis.

Subsequently, based on the Harmony-corrected low-dimensional embeddings, metacells (k = 25) were constructed within the same celltype and sample groups and were further normalized. After constructing the

expression matrix for network analysis, a signed network (networkType = "signed") was used to evaluate the fit of different soft-thresholding powers to scale-free topology using TestSoftPowers.

Based on the soft-threshold evaluation curve, a soft-thresholding power of $\beta = 10$ was selected to construct the weighted co-expression network. The minimum module size was set to 60 (minModuleSize = 60), the module merging threshold was set to 0.15 (mergeCutHeight = 0.15), and module detection was performed with deepSplit = 1.

Module eigengenes (MEs) were subsequently calculated and integrated at the sample level. Gene–module relationships were evaluated by calculating intramodular connectivity (kME), and modules were renamed accordingly. The top 25 hub genes in each module were selected to calculate module expression scores. Finally, UMAP embedding was performed based on the top 10 hub genes of each module (n_neighbors = 15, min_dist = 0.1) to visualize the co-expression network structure.

(5) Gene set activity scoring analysis:

To evaluate the activity of specific gene sets and signaling pathways at the single-cell level, the UCell method (v2.12.0) was applied for module scoring [39]. First, target gene sets (e.g., TNFSF10 downstream target genes) were organized into gene lists, and module scores were calculated based on the RNA expression matrix of the Seurat object.

In addition, KEGG pathway gene sets were obtained using KEGGREST (v1.48.1, https://doi.org/10.18129/B9.bioc.KEGGREST) (organism: human, organism = "hsa"), and the corresponding pathway gene lists (e.g., NF-κB signaling pathway, hsa04064) were extracted. Subsequently, pathway activity scores were calculated using the AddModuleScore_UCell function, and the scoring results were added to the Seurat object for downstream analysis and visualization.

(6) Transcription factor regulon activity analysis:

Transcription factor regulatory network analysis was performed based on the SCENIC framework [40]. First, gene filtering was performed on the expression matrix, retaining only genes expressed in ≥ 1% of cells, with total expression exceeding 3% of the number of cells, and present in the hg38 motif database.

Subsequently, pySCENIC (v0.12.1) was used for co-expression network construction, motif enrichment analysis, and regulon identification. Regulon activity (AUC) in each cell was calculated based on AUCell.

Further, in the R environment, regulon activity was extracted and visualized using SCENIC (v1.3.1)-related functions. Based on the regulon AUC matrix, a linear model (~ 0 + group) was constructed using limma to compare the dAMD and Control groups (contrast = "dAMD - Control"). Empirical Bayes moderation was performed using eBayes, and multiple testing correction was conducted using the Benjamini–Hochberg (BH) method. LogFC, P values, and FDR were extracted as the results of differential transcription factor activity analysis.

In addition, based on regulons obtained from pySCENIC, a one-sided Fisher's exact test (alternative = "greater") was performed to evaluate the enrichment of TNFSF10 target genes within transcription factor regulatory networks, using expressed genes in the target cell population as the background. Only regulons with ≥ 10 target genes were included in the analysis, and BH correction was applied for multiple testing. Transcription factors with FDR < 0.05 and overlapping gene number ≥ 10 were considered significantly enriched.

(7) Pseudotime analysis:

Pseudotime trajectory analysis was performed using Monocle 2 (R package monocle, v2.36.0) [41, 42]. First, the raw UMI count matrix was extracted from the Seurat object (assay = "RNA", slot = "counts") to construct a CellDataSet object. The expression distribution model was set according to the data type using a negative binomial model (negbinomial.size).

During preprocessing, estimateSizeFactors and estimateDispersions were applied to normalize gene expression and estimate dispersion. Genes with a minimum expression threshold of min_expr = 0.1, and expressed in at least 10 cells, were retained for subsequent analysis. The total UMI counts per cell (Total_mRNAs) were calculated, and cells with Total_mRNAs $\geq 1 \times 10^6$ were removed.

Ordering genes were selected through differentialGeneTest based on cell subpopulations, and genes with qval < 0.01 were used to construct the trajectory. Dimensionality reduction was performed using the DDRTree method (reduction_method = "DDRTree", max_components = 2), with batch variables incorporated into

the model (residualModelFormulaStr = "~sample", sigma = 0.1).

Cells were then ordered along pseudotime using orderCells, and the Monocyte subpopulation was defined as the root state. Finally, the two-dimensional trajectory coordinates calculated by Monocle 2 were integrated into the Seurat object's low-dimensional embeddings for visualization.

Results

Spatial transcriptomic analysis reveals myeloid cell accumulation and inflammatory activation in the RPE–choroid of PD mice

To characterize changes in the immune niche at the RPE–choroid interface in AMD, we reanalyzed a publicly available spatial transcriptomics dataset [17]. This dataset was generated from a photo-oxidative damage (PD) mouse model, which induces outer retinal degeneration and is widely used to model AMD [43]. The dataset includes dark-reared controls (DR, hereafter referred to as Control) and samples collected at days 1, 3, and 5 after PD exposure (Fig. 1A).

Unsupervised clustering of the spatial transcriptomic data identified major anatomical regions [44], including the ganglion cell layer (GCL), bipolar cell layer (BCL), photoreceptor layer (PRL), and the RPE–choroid region (Fig. 1C). These regions were annotated based on canonical marker gene expression [45, 46], such as Pou4f1 for ganglion cells (Fig. 1D; Supplementary Fig. S1). The spatial distribution of these regions across samples is shown in Fig. 1E.

To resolve cell-type composition across spatial locations, we integrated publicly available single-cell RNA-seq datasets as references and applied Robust Cell Type Decomposition (RCTD) for spatial deconvolution (Fig. 1F; Supplementary Fig. S2) [23, 25–27]. At 5 days after PD treatment, myeloid cell proportions were significantly increased in the RPE–choroid region compared to Control and showed pronounced enrichment toward the choroidal side, indicating an inflammatory activation state under injury conditions.

Gene Ontology (GO) enrichment analysis of differentially expressed genes (DEGs) between PD and Control within the RPE–choroid region revealed significant enrichment in inflammatory response [47], innate immune activation, and macrophage migration (Fig. 1H), further supporting an inflammatory activation state. Consistently, the macrophage marker Cd68 was upregulated in PD samples and predominantly localized to the RPE–choroid region (Fig. 1I) [48].

In conclusion, spatial transcriptomic analysis revealed that the RPE–choroid region exhibits pronounced myeloid cell accumulation accompanied by enhanced expression of inflammation-related genes in the PD model, suggesting that myeloid cells participate in local inflammatory responses.

Single-cell RNA-seq analysis reveals inflammatory activation and enhanced endothelial–myeloid interactions in dAMD

We integrated publicly available single-cell RNA-seq datasets of human RPE–choroid tissue (Fig. 2A), including healthy reference (HR, n = 12) and dry AMD (dAMD, n = 4) samples. UMAP-based clustering identified 11 major cell types, including RPE, endothelial, and myeloid cells (Fig. 2B), which were annotated based on canonical marker gene expression (Fig. 2D) [30, 49]. Cell proportion analysis revealed the presence of diverse immune cell populations across conditions (Fig. 2C).

Differential expression analysis demonstrated marked transcriptional changes across cell types in dAMD (Fig. 2E). Myeloid cells upregulated multiple genes, including ACOD1, NID1, KANK1, PPP1R13L, and SEPTIN4, among which NLRP3, a key component of the inflammasome [50], suggests activation of inflammatory responses. Meanwhile, endothelial cells upregulated multiple pro-inflammatory genes, including chemokines such as CXCL1 and CXCL3, suggesting activation of pro-inflammatory signaling. These findings suggest that endothelial cells may contribute to the activation of myeloid cells.

Enrichment analysis further supported these observations. Upregulated genes in endothelial cells were enriched in leukocyte chemotaxis, monocyte migration, and cell–matrix adhesion, as well as TNF and NF-κB signaling pathways (Fig. 2F). In contrast, upregulated genes in myeloid cells were enriched in inflammatory response and NF-κB signaling (Fig. 2G).

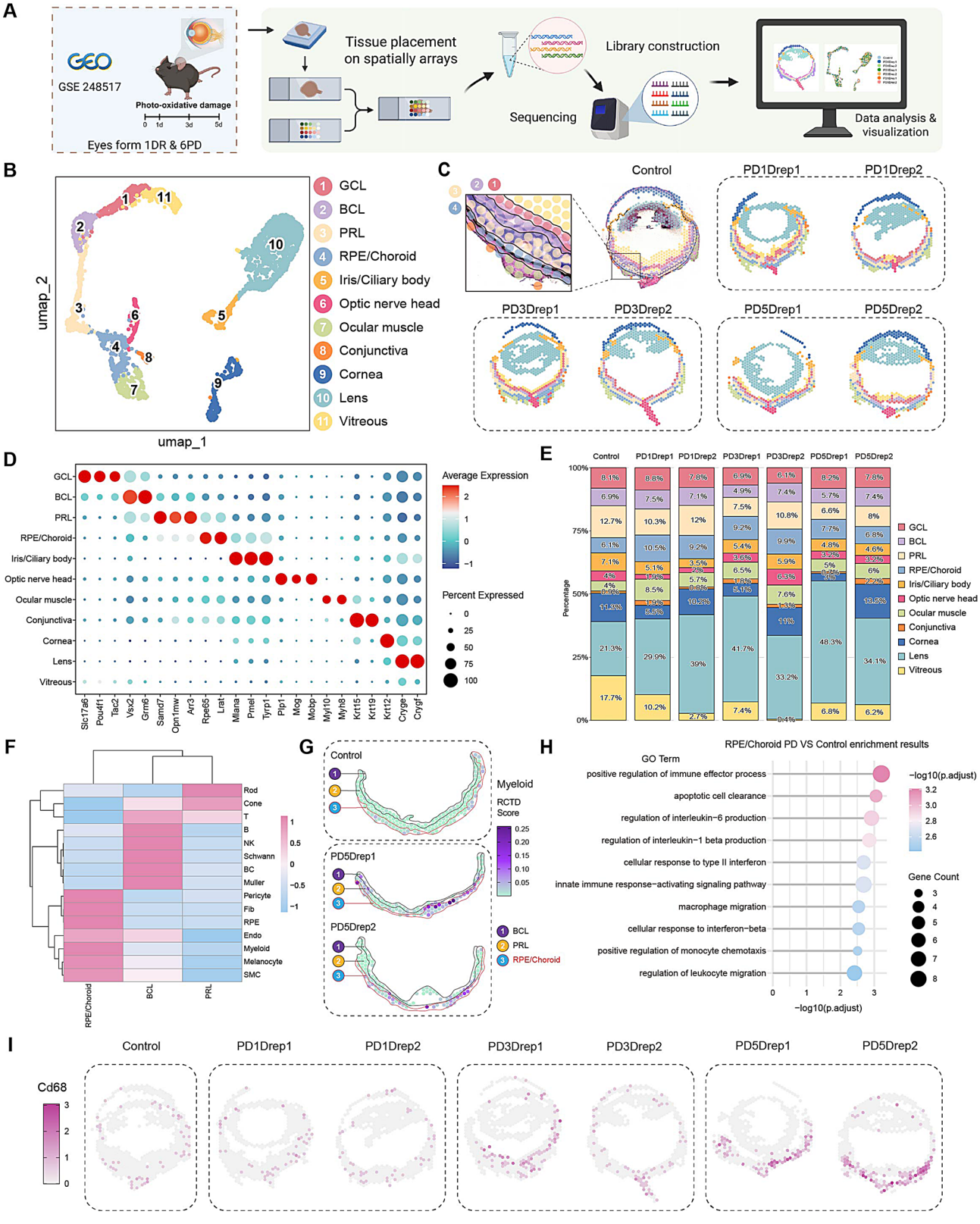

Fig. 1 (See legend on next page.)

(See figure on previous page.)

Fig. 1 Spatial transcriptomics reveals myeloid cell infiltration in the RPE/Choroid layer of PD mouse eyes. **(A)** Schematic representation of spatial transcriptomics (ST) analysis of whole eyes from dark-adapted control(Control) and photo-oxidative (PD 1-day、PD 3-day、PD 5-day) model mice, designed with BioRender (https://www.biorender.com/). **(B)** UMAP visualization showing diverse ocular cell lineages, highlighting distinct regional layers including ganglion cell layer（GCL）,bipolar cell layer（BCL）、PRL、retinal pigment epithelium/choroid (RPE/Choroid)、Iris/Ciliary body、Optic nerve head, Ocular muscle、Conjunctiva、Cornea、Lens、Vitreous. **(C)** Spatial plots illustrating the anatomical distribution of ocular regions in Control and PD1D, PD3D, PD5D mice.Colors for each region are consistent with the classification in panel **(B)**. **(D)** Bubble plot displaying the expression patterns of marker genes for distinct ocular regions in the spatial transcriptomics dataset.Dot color represents the average expression of genes within each region, while dot size reflects the percentage of spots expressing the gene. **(E)** Stacked bar plots showing the relative proportion of distinct ocular spatial regions in each sample from the Control and PD groups.Each vertical bar represents one sample, with colored segments corresponding to different spatial regions, and segment height indicating their relative proportion. **(F)** Heatmap illustrating the deconvolution scores of cell type composition across BCL, PRL, and RPE/Choroid regions, as inferred by RCTD from Visium spatial transcriptomics data. **(G)** Spatial feature plots showing the myeloid cell type scores inferred by RCTD.The upper panel shows one sample from the control group, and the lower panel shows two samples from the PD5D group. **(H)** Lollipop plots depicting the enrichment analysis of up-regulated genes in RPE/choroid in the PD group.The bar length indicates the enrichment significance of each term, while the adjacent dots represent the number of enriched genes, with dot size proportional to the gene count. **(I)** Spatial feature plots showing the spatial distribution of Cd68 expression in the standard Visium dataset. A common color scale was used across all 7 samples

We next analyzed cell–cell communication changes in dAMD using CellChat [34]. Compared to HR, overall interaction strength was increased among endothelial and myeloid cells with other cell types (Fig. 2H–I). Further analysis revealed that interactions from endothelial cells as senders to myeloid cells as receivers were specifically enhanced in dAMD (Fig. 2J).

In conclusion, single-cell analysis of the human RPE–choroid indicates that myeloid cells exhibit inflammatory activation in dAMD, while endothelial cells may drive myeloid activation through pro-inflammatory signaling, together contributing to a disease-promoting inflammatory niche.

A disease-associated SLC16A10^{+} pro-inflammatory macrophage subcluster in the dAMD niche

To further characterize myeloid cell activation in dAMD, the myeloid compartment was reclustered. UMAP visualization revealed four major subpopulations: monocytes, dendritic cells (DCs), SLC16A10^{-} macrophages, and SLC16A10^{+} macrophages (Fig. 3A), with corresponding marker gene expression shown in Fig. 3C. Notably, the proportion of SLC16A10^{+} macrophages was markedly increased in dAMD compared to controls (Fig. 3B), suggesting that this subcluster represents a disease-associated activated phenotype.

Functional annotation of DEGs in each subpopulation revealed that genes upregulated in SLC16A10^{+} macrophages were enriched in leukocyte migration and innate immune processes (Fig. 3D), indicating their role in shaping an inflammatory niche. To further characterize their transcriptional programs, gene co-expression networks were constructed using hdWGCNA [37], identifying nine modules (Fig. 3E). The co-expression network is visualized by UMAP (Fig. 3F), and module activity across myeloid subclusters is shown in Fig. 3H.

Modules 3, 5, and 8 were specifically enriched in SLC16A10^{+} macrophages (Fig. 3G). Enrichment analysis revealed strong associations with NF-κB signaling, TNF signaling, and immune/inflammatory processes (Fig. 3I), suggesting that this subcluster plays a central role in inflammatory regulation in dAMD.

In conclusion, reclustering of myeloid cells identified a disease-associated SLC16A10^{+} macrophage subcluster in dAMD. Combined transcriptional and pathway analyses indicate that this subcluster exhibits pronounced inflammatory activation and may function as a key effector population in dAMD progression.

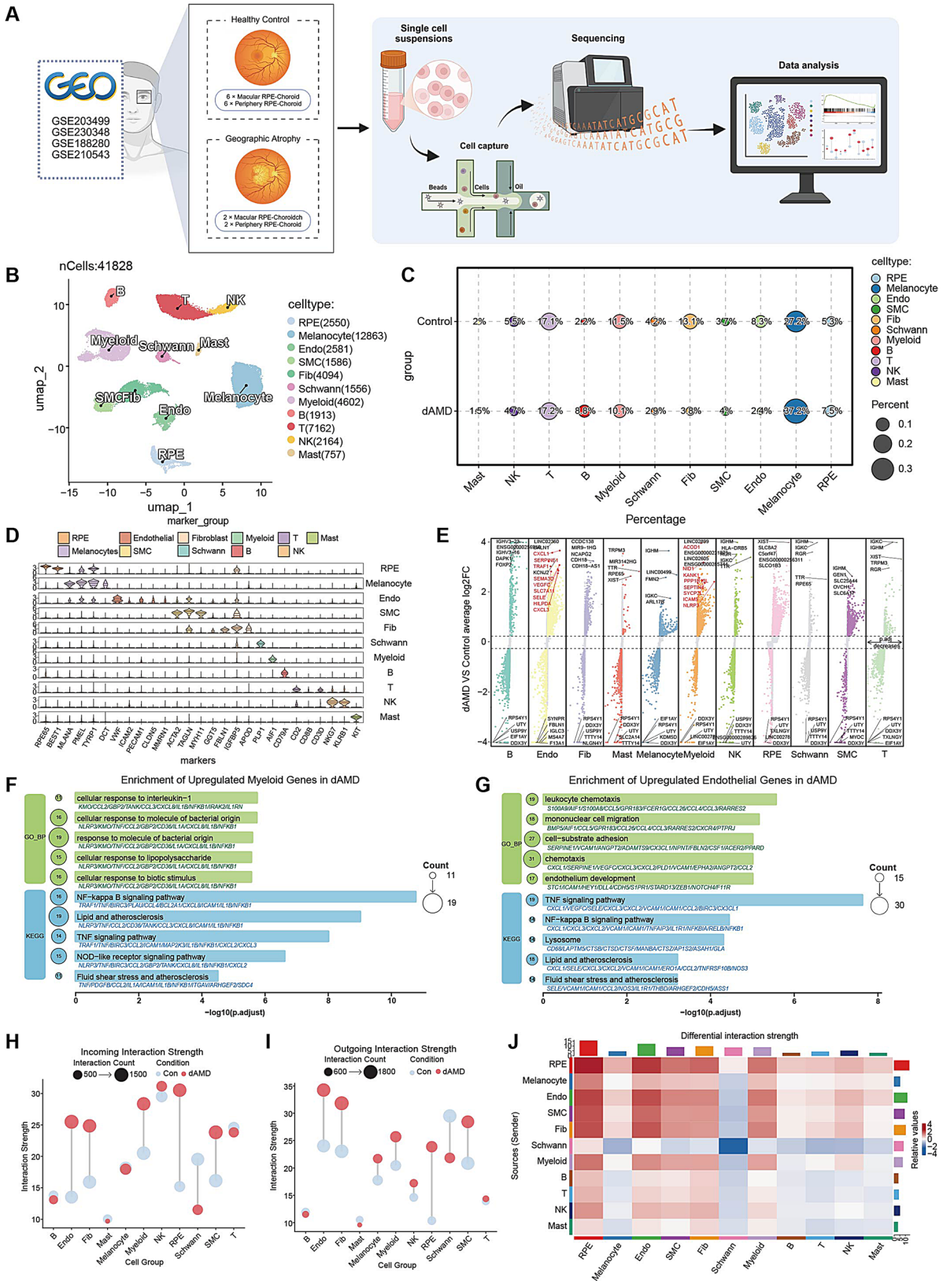

Fig. 2 (See legend on next page.)

(See figure on previous page.)

Fig. 2 Single-cell transcriptomic landscape and intercellular communication features in control and dry age-related macular degeneration (dAMD) RPE–choroid tissues. **(A)** Schematic overview of the single-cell RNA sequencing (scRNA-seq) workflow using macular and peripheral RPE–choroid tissues from control and dAMD samples. The illustration was created with BioRender. **(B)** UMAP visualization showing cellular heterogeneity within the RPE–choroid, identifying major cell populations including retinal pigment epithelial cells (RPE), melanocytes, endothelial cells (Endo), smooth muscle cells (SMC), fibroblasts (Fib), Schwann cells, myeloid cells, B cells, T cells, natural killer (NK) cells, and mast cells. **(C)** Bubble plot illustrating the relative proportions of major cell types between control and dAMD groups. Each dot represents the proportion of a specific cell type within a given group, with dot size indicating relative abundance. **(D)** Violin plots displaying canonical marker gene expression across major cell populations in the RPE–choroid. **(E)** Volcano plots illustrate the distribution of DEGs across major cell types in dAMD, with all genes shown as points. Selected representative genes are labeled, and key genes in endothelial and myeloid cells are highlighted in red. **(F)** Enrichment analysis of upregulated genes in endothelial cells from dAMD samples. Bar length reflects enrichment significance, whereas an adjacent dot column indicates the number of enriched genes, with dot size proportional to gene count. **(G)** Enrichment analysis of upregulated genes in myeloid cells from dAMD samples. Bar length reflects enrichment significance, whereas an adjacent dot column indicates the number of enriched genes, with dot size proportional to gene count. **(H)** Dumbbell plot depicting differences in incoming signaling strength among cell types between control and dAMD groups. Dot size indicates the number of inferred interactions. **(I)** Dumbbell plot showing differences in outgoing signaling strength among cell types between control and dAMD groups. Dot size indicates the number of inferred interactions. **(J)** Heatmap illustrating differential communication strength within identical cell types between control and dAMD conditions

Endothelial-derived TNFSF10–TNFRSF10B signaling recapitulates macrophage transcriptional programs and implicates NF-κB activation in dAMD

To further delineate the signaling mechanisms between endothelial cells and SLC16A10$^+$ macrophages, we systematically analyzed ligand–receptor interactions. Communication networks with endothelial cells as signal senders revealed that signaling toward SLC16A10$^+$ macrophages exhibited the highest interaction strength (Fig. 4A). Comparative analysis between HR and dAMD further showed that this interaction was markedly increased in dAMD (Fig. S3), indicating enhanced endothelial–macrophage crosstalk.

Differential analysis of candidate ligand–receptor pairs identified multiple altered interactions (Fig. 4B–C). By integrating cell type–specific expression patterns (Fig. 4D), the TNFSF10–TNFRSF10B signaling pathway was identified as the most specific interaction from endothelial cells to SLC16A10$^+$ macrophages [51, 52]. This pathway was globally strengthened in dAMD and predominantly enriched along the endothelial-to-SLC16A10$^+$ macrophage direction (Fig. 4E), suggesting its potential role in driving inflammatory responses.

To further evaluate the functional relevance of TNFSF10 signaling, we used NicheNet to predict its downstream target genes and constructed a TNFSF10 target gene set (Fig. 4F). This gene set was significantly enriched in dAMD SLC16A10$^+$ macrophages (Fig. 4G), accompanied by an increased TNFSF10 target program score (Fig. 4H).

Notably, enrichment analysis revealed that TNFSF10 target genes were primarily associated with inflammatory and stress-related pathways (Fig. 4I). Consistently, DEGs in dAMD SLC16A10$^+$ macrophages were also enriched in these pathways (Fig. 4J). Intersection analysis further identified a substantial overlap of enriched pathways between these two gene sets (Fig. 4K), indicating a strong concordance between TNFSF10 downstream signaling and the endogenous transcriptional program of SLC16A10$^+$ macrophages.

Together, these findings suggest that endothelial-derived TNFSF10 signaling closely recapitulates the intrinsic transcriptional programs of SLC16A10$^+$ macrophages. Enrichment of the NF-κB signaling pathway in both gene sets suggests that TNFSF10 signaling may promote inflammatory activation through NF-κB–dependent mechanisms.

NFKB1-mediated NF-κB signaling drives inflammatory transcriptional programs in dAMD SLC16A10$^+$ macrophages

To further investigate the transcriptional regulation downstream of TNFSF10 signaling, we performed SCENIC analysis focusing on transcription factors in SLC16A10$^+$ macrophages. Differential analysis showed that NFKB1, a key transcription factor mediating NF-κB signaling, was significantly upregulated in dAMD compared with the HR group (Fig. 5A). By assessing the overlap between TNFSF10 target genes and transcription factor regulons, we identified a set

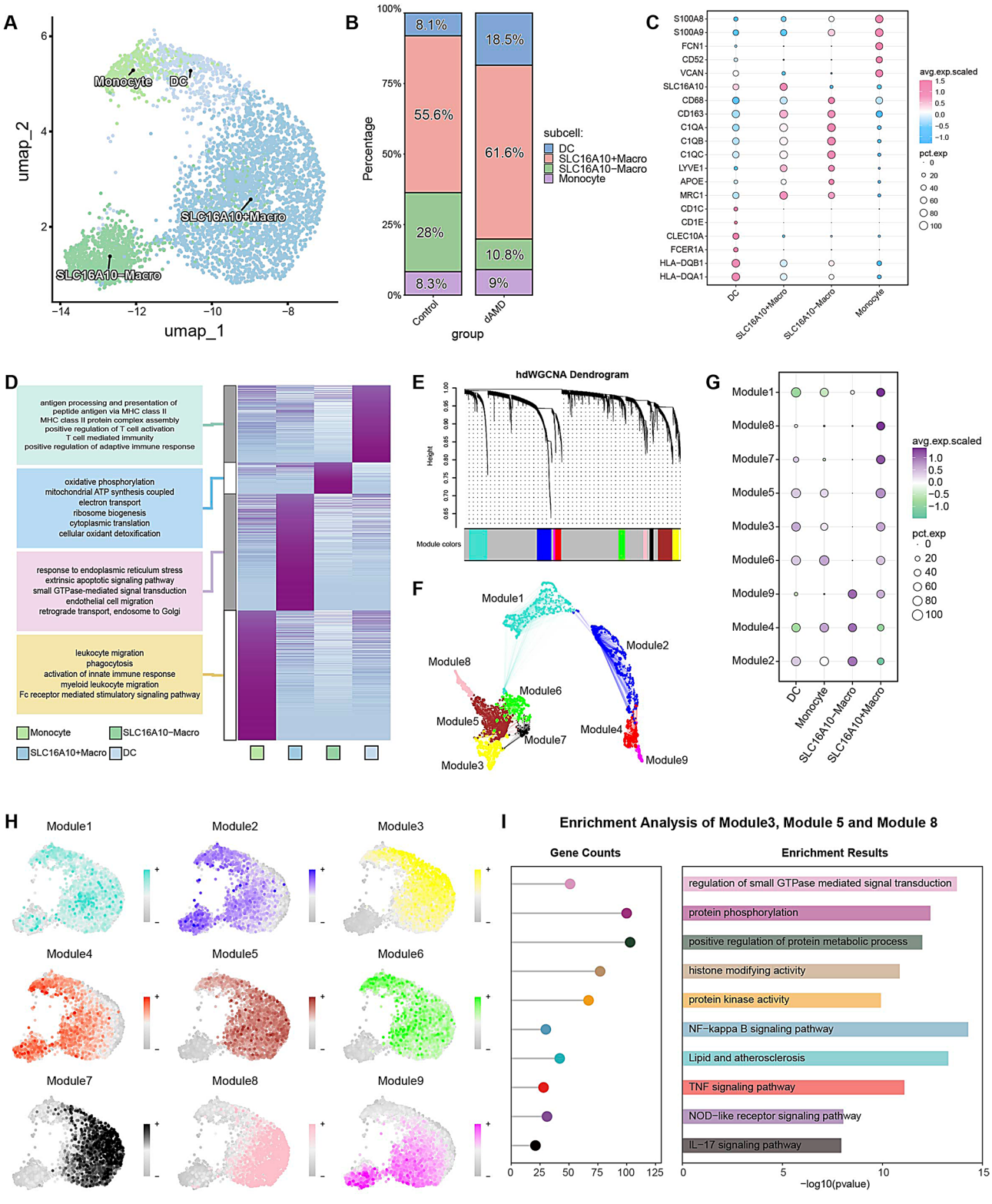

Fig. 3 (See legend on next page.)

(See figure on previous page.)

Fig. 3 Characterization of myeloid cell subpopulations and co-expression network analysis. **(A)** UMAP visualization of cellular heterogeneity within myeloid cells, identifying distinct subpopulations including monocytes, dendritic cells (DCs), SLC16A10-positive macrophages (SLC16A10$^+$ Macro), and SLC16A10-negative macrophages (SLC16A10$^-$ Macro). **(B)** Bar plot showing the relative proportions of myeloid subpopulations between control and dAMD groups. **(C)** Bubble plot displaying marker gene expression patterns across myeloid subpopulations. Dot color represents the average expression level of each gene within the corresponding cell type, and dot size indicates the proportion of cells expressing the gene. **(D)** Heatmap showing enrichment analysis of DEGs among myeloid subpopulations. Enrichment results are presented as horizontal bands, with only selected representative functional terms annotated. **(E)** hdWGCNA gene dendrogram illustrating nine co-expression modules constructed based on gene functional relationships. Each module is indicated by a distinct color. Each leaf of the dendrogram represents a gene, and the color bar below denotes module assignment. The gray module contains genes not assigned to any co-expression module and is excluded from downstream analyses. **(F)** UMAP visualization of the co-expression network. Each node represents a gene, and edges indicate co-expression relationships with module hub genes. Node size is scaled according to kME values, and nodes are colored by module assignment. **(G)** Bubble plot showing module expression patterns across four myeloid subpopulations. **(H)** UMAP projection displaying the expression distribution of modules within myeloid cells. **(I)** Enrichment analysis of Module3, Module5 and Module8 genes. The left lollipop plot represents the number of enriched genes, while the right bar plot shows enriched pathways, with bar length reflecting enrichment significance

of TNFSF10-associated transcription factors (Fig. 5B). Intersection with transcription factors upregulated in dAMD revealed that NFKB1 was included in the overlap and exhibited significantly increased activity (Fig. 5C–D), indicating its potential role as a central regulator of TNFSF10-associated transcriptional programs.

A regulatory network centered on NFKB1 was constructed (Fig. 5E), revealing associations with multiple inflammation- and signaling-related genes, including TANK, TRAF3, and CFLAR. Consistently, NFKB1 expression was elevated in dAMD SLC16A10$^+$ macrophages, accompanied by increased NF-κB signaling pathway activity (Fig. 5F–G).

These findings indicate that NFKB1 links TNFSF10 signaling to NF-κB pathway activation in dAMD SLC16A10$^+$ macrophages.

Progressive activation of NF-κB signaling during monocyte-to-SLC16A10$^+$ macrophage differentiation

To investigate the differentiation trajectory of SLC16A10$^+$ macrophages in dAMD, pseudotime analysis was performed on myeloid cells. Trajectory inference revealed that monocytes were positioned at the root and diverged into two major branches (Fig. 6A–B), with one branch predominantly enriched for SLC16A10$^+$ macrophages and the other mainly comprising SLC16A10$^-$ macrophages.

Clustering of pseudotime-associated genes identified four gene modules (C1–C4) (Fig. 6C). Notably, specific modules (e.g., cluster 2 and cluster 4) were upregulated along the lineage corresponding to SLC16A10$^+$ macrophages (Lineage 2) and were enriched in inflammation-related pathways, including NF-κB signaling and TNF signaling pathways.

To assess dynamic changes in NF-κB signaling along the differentiation trajectory, an NF-κB signaling pathway score was calculated and projected onto the pseudotime space. The results showed a progressive increase in NF-κB pathway activity along the SLC16A10$^+$ macrophage lineage (Fig. 6D). Consistently, NFKB1 expression gradually increased along this branch, whereas it exhibited a declining trend along the alternative lineage (Fig. 6E).

Collectively, pseudotime analysis indicates that the differentiation of SLC16A10$^+$ macrophages is accompanied by enrichment of inflammation-associated gene modules, together with progressive upregulation of NFKB1 expression and NF-κB signaling activity. These findings suggest

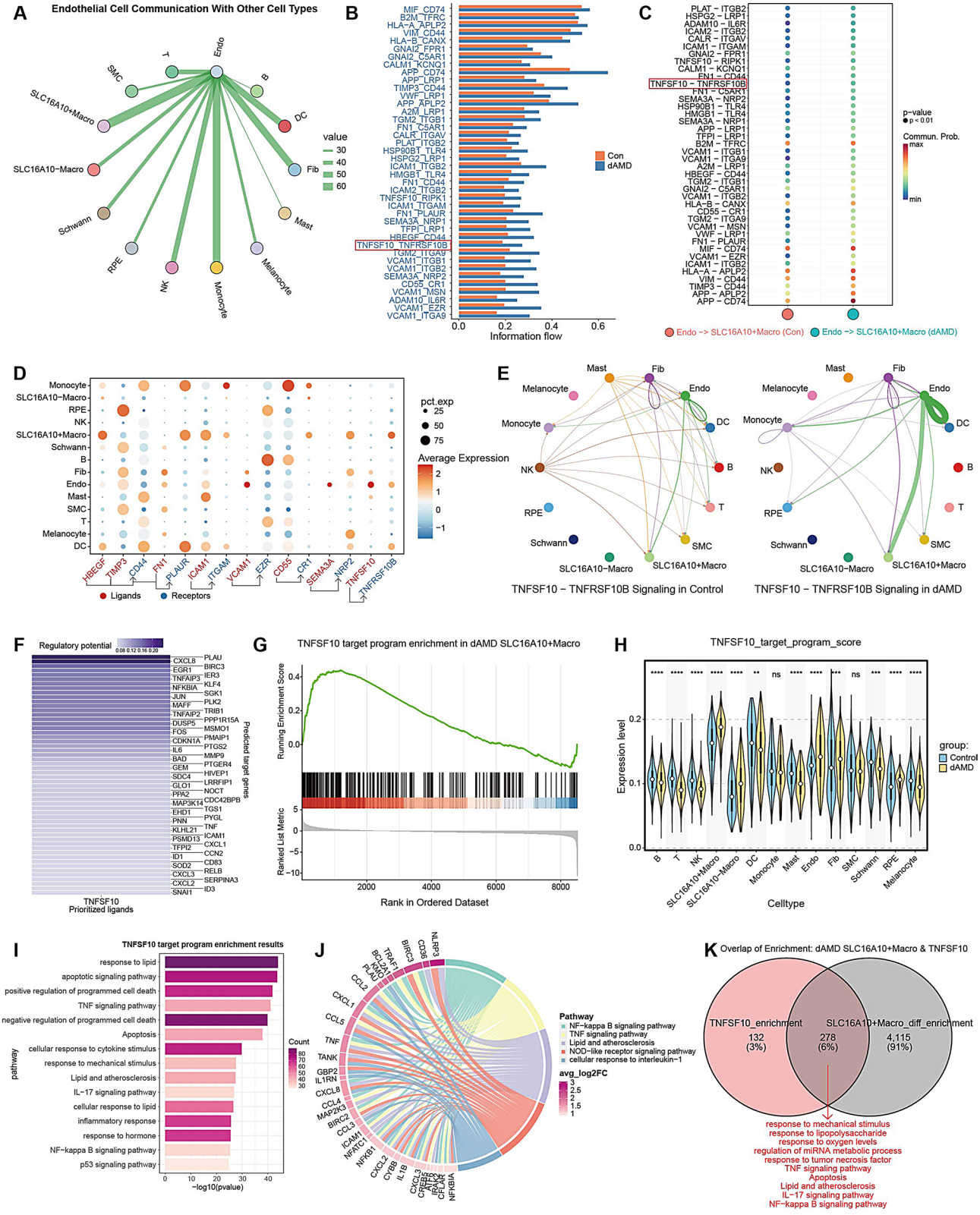

Fig. 4 (See legend on next page.)

(See figure on previous page.)

Fig. 4 TNFSF10–TNFRSF10B–mediated endothelial–SLC16A10$^+$ macrophage communication and functional characterization. **(A)** Circular network plot illustrating intercellular communication centered on endothelial cells. Nodes represent distinct cell types and are colored by cell category; edges indicate inferred ligand–receptor interactions, with edge width reflecting communication strength (number of ligand–receptor pairs). **(B)** Bar plot showing the top 40 upregulated ligand–receptor pairs in the dAMD group ranked by communication probability (prob). The ligand–receptor pair TNFSF10–TNFRSF10B of particular interest is highlighted with a red box. **(C)** Bubble plot comparing ligand–receptor interactions between endothelial cells and SLC16A10$^+$ macrophages in Control and dAMD groups. Bubble size represents statistical significance (p value, $p < 0.01$), while bubble color denotes communication probability. The TNFSF10–TNFRSF10B pair is highlighted with a red box. **(D)** Bubble plot depicting gene expression patterns of ligand–receptor pairs across major cell types. Dot color indicates average gene expression within each cell type, and dot size reflects the proportion of cells expressing the gene. Ligands and receptors are annotated according to the legend. **(E)** Circular network plot showing signaling strength of the TNFSF10–TNFRSF10B ligand–receptor pair in Control and dAMD groups. Nodes represent cell types, and edges denote ligand–receptor–mediated signaling. Edge color indicates signal source, and edge width reflects communication weight. Edge widths were normalized using a shared maximum value across groups to enable comparison. **(F)** Heatmap displaying the regulatory potential of ligand TNFSF10 on predicted target genes. Rows represent ligands and columns represent filtered predicted target genes, with color intensity indicating regulatory strength. **(G)** GSEA enrichment plot showing enrichment of the TNFSF10 target gene program (TNFSF10_target_program) in dAMD SLC16A10$^+$ macrophages. The curve represents the running enrichment score, and the peak reflects the degree of enrichment within the ranked gene list. Analysis was performed using the top 300 TNFSF10 target genes ranked by NicheNet-predicted regulatory potential. **(H)** Module activity of the TNFSF10 target gene program in RPE–choroid cell types assessed by UCell scoring. Violin plots show score distributions across Control and dAMD groups, with colors indicating group identity. Statistical comparisons are annotated (ns: $p > 0.05$; *: $p \le 0.05$; **: $p \le 0.01$; ***: $p \le 0.001$; ****: $p \le 0.0001$), reflecting activity differences between groups. **(I)** Bar plot showing enrichment results of the TNFSF10 target gene program. Bar length represents significance (− log10 p value), and color indicates the number of enriched genes, with deeper color corresponding to higher gene counts. **(J)** Chord diagram illustrating enriched pathways of DEGs in SLC16A10$^+$ macrophages in dAMD versus Control and their associated genes. Links represent pathway–gene associations with directionality from pathways to genes. Pathway nodes are colored by category, and gene nodes are colored according to expression change in dAMD (avg_log2FC). **(K)** Venn diagram displaying pathway overlap between enrichment results of the TNFSF10 target gene program and enrichment results of DEGs in SLC16A10$^+$ macrophages (dAMD vs. Control). Numbers indicate pathway counts and intersections, with proportional percentages annotated for each region. Representative overlapping GO and KEGG pathways are highlighted in red

that SLC16A10$^+$ macrophages may respond to endothelial–macrophage crosstalk through NF-κB–mediated inflammatory signaling, thereby contributing to immune niche remodeling and disease-associated inflammation in dAMD.

Discussion

Age-dependent, progressive degeneration of the outer retina, encompassing the retinal pigment epithelium (RPE) and choroid, constitutes a hallmark pathological feature of dry age-related macular degeneration (dAMD) [2, 49, 53, 54], with chronic inflammation serving a central pathogenic role [55, 56]. In this study, we innovatively integrated single-cell and spatial analyses to elucidate the mechanisms underlying inflammatory niche formation in the outer retina. Using spatial transcriptomics, we first identified myeloid cell infiltration as a key pro-inflammatory alteration in the RPE-choroid niche of a photo-oxidation mouse model. We subsequently demonstrated that endothelial cell-derived TNFSF10 activates SLC16A10$^+$ macrophages via TNFRSF10B/NF-κB signaling, driving the release of inflammatory cytokines and establishment of a pro-inflammatory niche.

Several prior studies have employed light-induced oxidative damage to generate mouse models recapitulating the human dAMD phenotype [57, 58]. In the present work, PD 1D mice, which approximate an early-stage AMD phenotype [59], exhibited no substantial myeloid cell aggregation in the RPE/choroid (Supplementary Fig. 1), whereas PD5D mice displayed marked choroidal myeloid infiltration and elevated expression of the monocyte/macrophage marker CD68 (Fig. 1), implicating myeloid cells in advanced AMD progression within this region. While retinal microglia (a myeloid subcluster) have been extensively studied [60–62], choroidal macrophage populations have received less attention, with most studies focusing on nAMD [63–65]. Thus, a more comprehensive investigation of dAMD-associated macrophages is warranted.

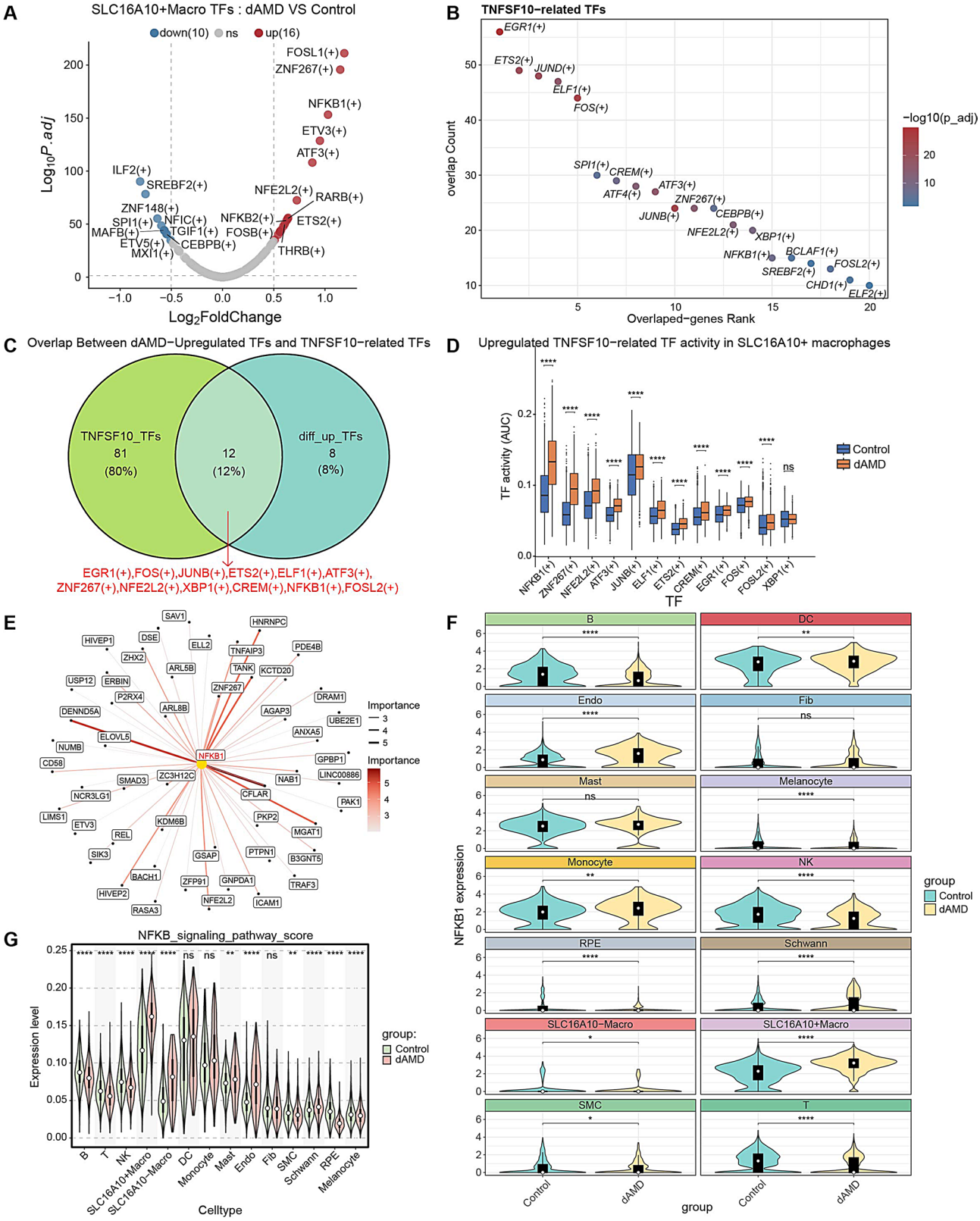

Fig. 5 (See legend on next page.)

(See figure on previous page.)

Fig. 5 Characteristics of dAMD-associated transcription factors and NF-κB signaling pathway in SLC16A10⁺ macrophages. **(A)** Volcano plot showing differentially expressed transcription factors (TFs) between dAMD and control groups in SLC16A10⁺ macrophages. Each point represents a TF, with the x-axis indicating $\log_2$ fold change ($\log_2$FC) and the y-axis showing $-\log_{10}$ adjusted p value. TFs meeting the significance threshold (FDR < 0.05 and $|\log_2 FC| > 0.5$) are labeled, with upregulated TFs in dAMD shown in red, downregulated TFs in blue, and non-significant TFs in gray. **(B)** Rank plot displaying the top 20 representative TF regulons associated with TNFSF10 and their significant overlap with TNFSF10 target genes. The x-axis represents TFs ranked by the number of overlapping genes, and the y-axis indicates the number of overlapping genes. The color of each point reflects the enrichment significance ($-\log_{10}$ adjusted p value), with deeper colors indicating higher significance. **(C)** Venn diagram showing the overlap between upregulated TFs in dAMD (diff_up_TFs) and TNFSF10-related TFs (TNFSF10_TFs). Numbers indicate the size of each group and their intersection, with percentages representing the proportion of each part. TFs in the intersection are highlighted in red. **(D)** Boxplot illustrating the regulatory activity (AUC) of core TFs that are both upregulated in dAMD and TNFSF10-related (up_overlap_TFs) in SLC16A10⁺ macrophages from control and dAMD groups. Statistical comparisons between groups are indicated. **(E)** Regulatory network of the top 50 target genes controlled by NFKB1, with edges representing regulatory strength. Nodes represent TFs or target genes, with NFKB1 highlighted in yellow and target genes in black. Edge width and color indicate regulatory strength, with color intensity reflecting the magnitude. **(F)** Violin plot showing the expression of NFKB1 across different cell types in control and dAMD groups. Each violin represents the expression distribution within a cell type, with median values indicated by boxplots and colors distinguishing groups. Statistical comparisons between groups are indicated. **(G)** Violin plot showing the activity scores of the NF-κB signaling pathway across different cell types in control and dAMD groups. Each violin represents the distribution of pathway scores for a given cell type, with median values indicated by boxplots, colors distinguishing groups, and statistical comparisons annotated

In-depth analysis of human RPE-choroid scRNA-seq data revealed substantial transcriptional alterations in the myeloid cell compartment of dAMD samples, accompanied by significantly enhanced incoming signaling from other cell populations (Fig. 2). Myeloid cells are characterized by diversity and plasticity, enabling the generation of subclusters with distinct molecular phenotypes and functions in response to various stimuli [66, 67]. Traditionally, macrophages have been dichotomized into pro-inflammatory (M1) and anti-inflammatory (M2) subclusters [68, 69]. Here, based on SLC16A10 expression, we designated the two identified macrophage subclusters as SLC16A10⁻ and SLC16A10⁺ macrophages. SLC16A10⁻ macrophages are primarily engaged in metabolism and protein synthesis, supporting tissue homeostasis and repair. In contrast, SLC16A10⁺ macrophages exhibited pronounced pro-inflammatory, stress-response, and vascular-migration signatures, with enrichment of classic inflammatory pathways such as NF-κB, indicative of an activated state central to tissue injury, oxidative stress, and the formation of a complex vascular-inflammatory niche (Fig. 3). This subcluster may thus represent a key target for impeding dAMD progression. Notably, strong endothelial-to-macrophage signaling was markedly enhanced in dAMD (Fig. 4). Endothelial degeneration, an early event in AMD pathogenesis [70, 71], has also been shown to critically regulate macrophages in various vascular and inflammatory diseases [72, 73]. Collectively, these findings underscore endothelial-SLC16A10⁺ macrophage crosstalk within the vascular-inflammatory niche as a pivotal driver of dAMD progression.

We identified TNFSF10/TNFRSF10B signaling as a key conduit for endothelial regulation of SLC16A10⁺ macrophages, with NF-κB serving as the critical downstream pathway. Endothelial cell-derived TNFSF10 interaction with TNFRSF10B on SLC16A10⁺ macrophages was significantly augmented in dAMD (Fig. 4). We propose that during dAMD pathogenesis, endothelial TNFSF10 engages TNFRSF10B on SLC16A10⁺ macrophages, activating NF-κB signaling and inducing robust pro-inflammatory cytokine release, thereby perpetuating a sustained inflammatory niche. TNFSF10, a TNF superfamily member traditionally associated with apoptosis induction [74–76], has been reported to regulate angiogenesis, cell recruitment, and vascular stabilization when derived from endothelial cells [77], with emerging roles in inflammation control [78, 79]. Prior work demonstrated that anti-TNFSF10 therapy suppresses retinal

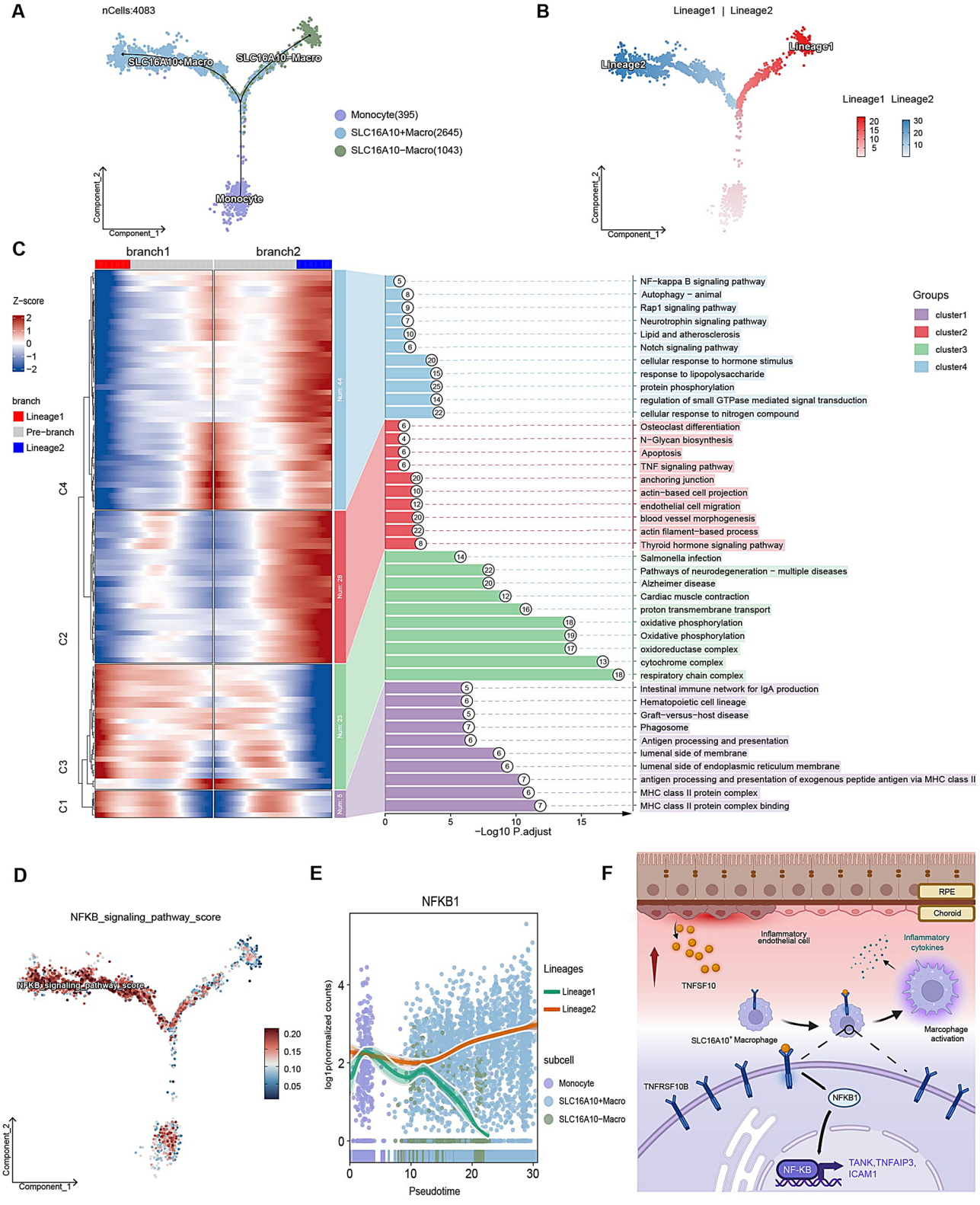

Fig. 6 (See legend on next page.)

(See figure on previous page.)

Fig. 6 Dynamics of myeloid cell subtypes. **(A)** Pseudotime trajectory analysis showing the developmental dynamics of three myeloid subtypes, with distinct colors representing different cell subclusters and arrows indicating the end points of the trajectory. **(B)** Pseudotime lineage trajectory showing distinct developmental lineages of myeloid cell populations. **(C)** Heatmap (right) depicting the dynamic changes in gene expression along the pseudotime trajectory. Genes within the trajectory were partitioned into four distinct modules. Corresponding enrichment analysis results for each module are shown on the left, where bar length represents the enrichment significance, and the numbers within adjacent circles indicate the number of enriched genes. **(D)** Feature plot illustrating the dynamic changes in the NF-κB signaling pathway score across the pseudotime trajectory. **(E)** Gene expression of NFKB1 over pseudotime.Scatter points are colored by distinct myeloid cell subtypes, and curves are colored by different lineages. **(F)** Schematic illustration of the endothelial–macrophage TNFSF10–NF-κB signaling pathway in dAMD

inflammation in age-related disease models by modulating inflammatory and anti-inflammatory microglia [80], consistent with our findings and supporting TNFSF10 as a therapeutic target in dAMD. NFKB1, a core NF-κB family member, orchestrates inflammatory responses and drives expression of multiple inflammation-related genes in SLC16A10⁺ macrophages (Fig. 5) [81], further corroborating NF-κB pathway activation in this subcluster. Pseudotime analysis revealed that the differentiation trajectory of SLC16A10⁺ macrophages involves progressively increasing NFKB1 expression and NF-κB pathway activity (Fig. 6), suggesting that activation of inflammatory programs is an acquired feature during subcluster divergence. These results provide evidence for endothelial TNFSF10 paracrine signaling promoting pro-inflammatory activation in SLC16A10⁺ macrophages via NF-κB, while expanding our understanding of TNFSF10 function in dAMD pathology.

Based on these findings, we propose a schematic model in which endothelial-derived TNFSF10 activates SLC16A10⁺ macrophages through TNFRSF10B, leading to NFKB1-mediated NF-κB signaling and subsequent pro-inflammatory activation (Fig. 7). This process drives inflammatory remodeling of the RPE–choroid niche and contributes to dAMD progression.

In summary, by integrating scRNA-seq and spatial transcriptomics data, this study systematically maps the remodeling of the RPE-choroid niche in dAMD. We identify SLC16A10⁺ macrophages as a pro-inflammatory dAMD-associated subcluster whose inflammatory activation is closely tied to endothelial-derived TNFSF10 signaling and NFKB1-mediated transcriptional regulation. These findings offer new cellular and molecular insights into how the RPE-choroid inflammatory niche contributes to dAMD progression, and provide a theoretical foundation for interventions targeting the endothelial-macrophage TNFSF10/TNFRSF10B/NF-κB pathway.

Conclusions

This study systematically characterizes immune remodeling in the RPE–choroid region in dry AMD and identifies an endothelial–macrophage TNFSF10–TNFRSF10B–NF-κB signaling pathway that drives disease progression. These findings provide new insights into disease mechanisms and suggest potential therapeutic targets for dry AMD.

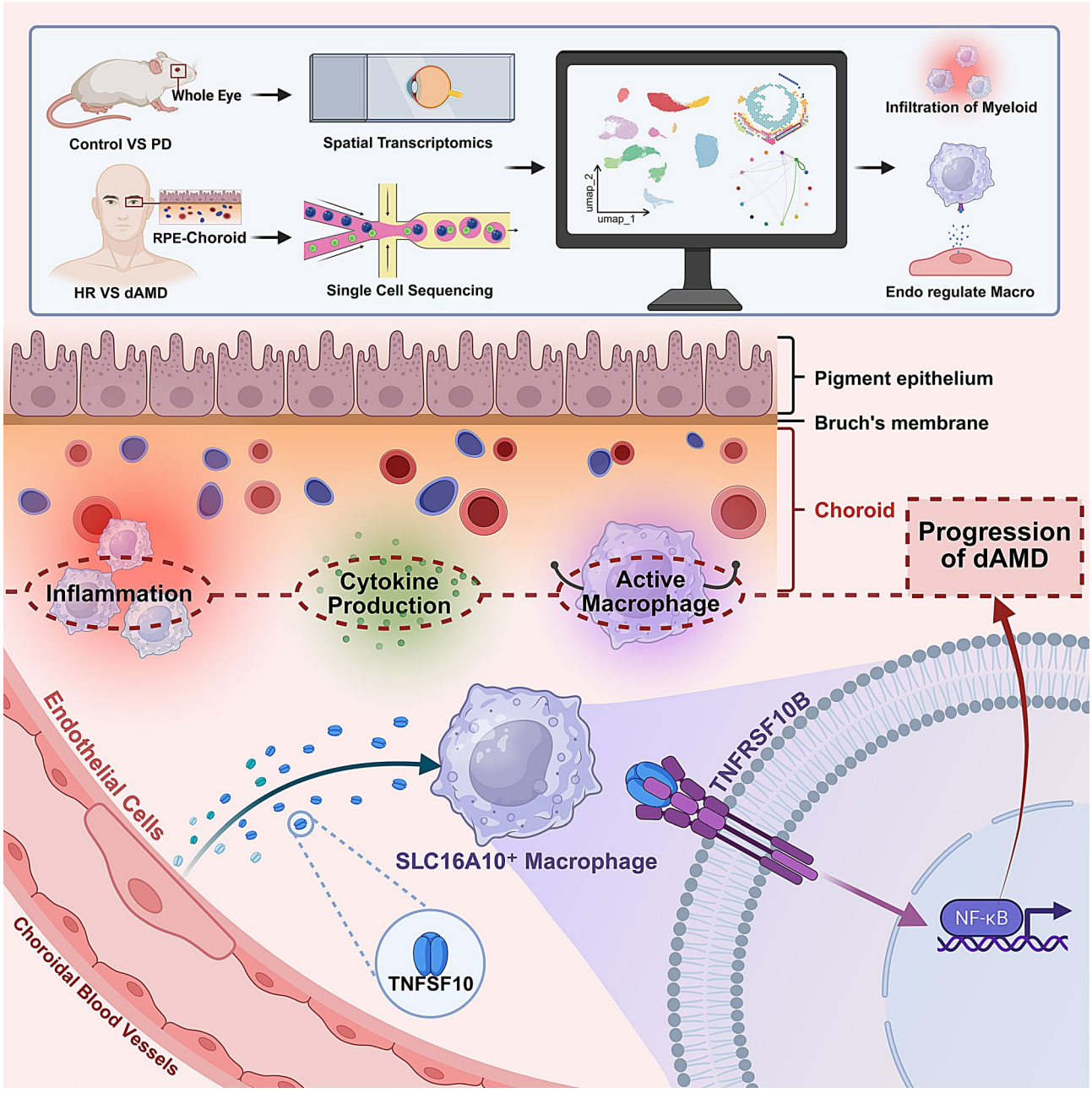

Fig. 7 Proposed model of the endothelial–macrophage TNFSF10–TNFRSF10B–NFKB1–NF-κB signaling pathway driving inflammatory remodeling in dAMD. By integrating spatial transcriptomics and single-cell RNA sequencing, this study identifies an endothelial–macrophage TNFSF10–TNFRSF10B–NF-κB signaling pathway as a key driver of inflammation in the RPE–choroid microenvironment in dAMD. Activation of this pathway promotes pro-inflammatory polarization of SLC16A10⁺ macrophages and drives inflammatory remodeling of the local niche, thereby contributing to disease progression. Targeting this signaling cascade may represent a potential therapeutic strategy for dAMD

Abbreviations

AMD	Age-related macular degeneration
dAMD	Dry age-related macular degeneration
GA	Geographic atrophy
RPE	Retinal pigment epithelium
PD	Photo-oxidative damage
scRNA-seq	Single-cell RNA sequencing
RCTD	Robust Cell Type Decomposition
DEG	Differentially expressed gene
GO	Gene Ontology
UMAP	Uniform Manifold Approximation and Projection
HR	Healthy reference
DC	Dendritic cell
nAMD	Neovascular age-related macular degeneration
NF-κB	Nuclear factor kappa B

Supplementary Information

The online version contains supplementary material available at https://doi.org/10.1186/s12967-026-08393-7.

Supplementary Material 1

Supplementary Material 2

Supplementary Material 3

Supplementary Material 4

Acknowledgements
Not applicable.

Author contributions
Y.W. conceived the study; L.C., Y.Z., and Y.W. designed the study; Y.C., C.L. analyzed the single-cell transcriptomics data and J.C. analyzed the spatial transcriptomics data; Y.C., C.L., J.C., YM.H., G.P., P.W. and YS.H. made the figures; Y.C., C.L., J.C. and YM.H. drafted and revised the paper; all authors approved the final version of the paper.

Funding
Not applicable.

Data availability
This study utilized raw transcriptomic data, including single-cell RNA sequencing and spatial transcriptomics data, all of which were obtained from the Gene Expression Omnibus (GEO, http://www.ncbi.nlm.nih.gov/geo/). Detailed information is provided in the Supplementary Materials.

Declarations

Ethics approval and consent to participate
Not applicable.

Consent for publication
Not applicable.

Competing interests
The authors declare no competing interests.

Author details
[1]Medical School, Shenzhen University, Shenzhen, China
[2]Nanfang Hospital, Southern Medical University, Guangzhou, Guangdong, China
[3]The First School of Clinical Medicine, Southern Medical University, Guangzhou, Guangdong, China
[4]Department of Ophthalmology, South China Hospital, Medical School, Shenzhen University, Shenzhen, China
[5]Department of Anesthesiology, Southern University of Science and Technology Hospital, Shenzhen, Guangdong, China
[6]State Key Laboratory of Multi-Organ Injury Prevention and Treatment, Division of Nephrology, Nanfang Hospital, National Clinical Research Center of Kidney Disease, Southern Medical University, Guangzhou, China
[7]Guangdong Provincial Key Laboratory of Renal Failure Research, Guangdong Provincial Institute of Nephrology, Guangzhou, China

Received: 27 May 2026 / Accepted: 29 May 2026
Published online: 16 June 2026

References

1. Velez-Montoya R, Oliver SC, Olson JL, Fine SL, Quiroz-Mercado H, Mandava N. Current knowledge and trends in age-related macular degeneration: genetics, epidemiology, and prevention. Retina. 2014;34(3):423–41.
2. Guymer RH, Campbell TG. Age-related macular degeneration. Lancet. 2023;401(10386):1459–72.
3. Wong WL, Su X, Li X, Cheung CM, Klein R, Cheng CY, et al. Global prevalence of age-related macular degeneration and disease burden projection for 2020 and 2040: a systematic review and meta-analysis. Lancet Glob Health. 2014;2(2):e106–16.
4. Fleckenstein M, Keenan TDL, Guymer RH, Chakravarthy U, Schmitz-Valckenberg S, Klaver CC, et al. Age-related macular degeneration. Nat Rev Dis Primers. 2021;7(1):31.
5. Swaroop A, Chew EY, Rickman CB, Abecasis GR. Unraveling a multifactorial late-onset disease: from genetic susceptibility to disease mechanisms for age-related macular degeneration. Annu Rev Genomics Hum Genet. 2009;10:19–43.
6. Bhutto I, Lutty G. Understanding age-related macular degeneration (AMD): relationships between the photoreceptor/retinal pigment epithelium/Bruch's membrane/choriocapillaris complex. Mol Aspects Med. 2012;33(4):295–317.
7. Chen M, Xu H. Parainflammation, chronic inflammation, and age-related macular degeneration. J Leukoc Biol. 2015;98(5):713–25.
8. Armento A, Ueffing M, Clark SJ. The complement system in age-related macular degeneration. Cell Mol Life Sci. 2021;78(10):4487–505.
9. Delrue C, Speeckaert R, Speeckaert MM. Molecular crosstalk in age-related macular degeneration: integrating oxidative stress, inflammation, microRNAs, and genetic susceptibility toward precision therapeutics. Biomolecules. 2026;16(2).
10. Zhang Y, Wong WT. Innate Immunity in Age-Related Macular Degeneration. Adv Exp Med Biol. 2021;1256:121–41.
11. Arya M, Sabrosa AS, Duker JS, Waheed NK. Choriocapillaris changes in dry age-related macular degeneration and geographic atrophy: a review. Eye Vis (Lond). 2018;5:22.
12. Kim JT, Jun JH, Lee SC, Lee MW. Retinal microvasculature and choriocapillaris impairments according to the stage of dry age-related macular degeneration. Clin Exp Ophthalmol. 2023;51(1):36–43.
13. Mullins RF, Johnson MN, Faidley EA, Skeie JM, Huang J. Choriocapillaris vascular dropout related to density of drusen in human eyes with early age-related macular degeneration. Invest Ophthalmol Vis Sci. 2011;52(3):1606–12.
14. Pober JS, Sessa WC. Evolving functions of endothelial cells in inflammation. Nat Rev Immunol. 2007;7(10):803–15.
15. Guan Y, Racioppi L, Gerecht S. Engineering biomaterials to tailor the microenvironment for macrophage–endothelium interactions. Nat Reviews Mater. 2023;8(10):688–99.
16. Borchert GA, Charbel Issa P, Xue K, MacLaren RE, Cehajic-Kapetanovic J, Downes SM, et al. Geographic atrophy in age-related macular degeneration: phenotypic characterisation for clinical trial consideration. Graefes Arch Clin Exp Ophthalmol. 2026.
17. Schumann U, Liu L, Aggio-Bruce R, Cioanca AV, Shariev A, Madigan MC, et al. Spatial transcriptomics reveals regionally altered gene expression that drives retinal degeneration. Commun Biol. 2025;8(1):629.
18. Hao Y, Hao S, Andersen-Nissen E, Mauck WM 3rd, Zheng S, Butler A, et al. Integrated analysis of multimodal single-cell data. Cell. 2021;184(13):3573–e8729.
19. Larsson L, Franzén L, Ståhl PL, Lundeberg J. Semla: a versatile toolkit for spatially resolved transcriptomics analysis and visualization. Bioinformatics. 2023;39(10).
20. Choudhary S, Satija R. Comparison and evaluation of statistical error models for scRNA-seq. Genome Biol. 2022;23(1):27.
21. McInnes L, Healy J. UMAP: uniform manifold approximation and projection for dimension reduction. ArXiv. 2018. abs/1802.03426.
22. Ginestet C. J ggplot2: elegant graphics for data analysis. Royal Stat Soc Ser A: Stat Soc. 2011;174(1):245–6.
23. Cable DM, Murray E, Zou LS, Goeva A, Macosko EZ, Chen F, et al. Robust decomposition of cell type mixtures in spatial transcriptomics. Nat Biotechnol. 2022;40(4):517–26.
24. Yu G, Wang LG, Han Y, He QY. clusterProfiler: an R package for comparing biological themes among gene clusters. Omics. 2012;16(5):284–7.
25. Dong X, Song Y, Wang X, Yan H. Natural killer cells cooperate with neutrophils to suppress pathological angiogenesis in neovascular age-related macular degeneration. Investig Ophthalmol Vis Sci. 2023;64(8):3908.
26. Droho S, Voigt AP, Sterling JK, Rajesh A, Chan KS, Cuda CM, et al. NR4A1 deletion promotes pro-angiogenic polarization of macrophages derived from classical monocytes in a mouse model of neovascular age-related macular degeneration. J Neuroinflammation. 2023;20(1):238.
27. Droho S, Rajesh A, Cuda CM, Perlman H, Lavine JA. CD11c+ macrophages are proangiogenic and necessary for experimental choroidal neovascularization. JCI Insight. 2023;8(7).
28. Germain PL, Lun A, Garcia Meixide C, Macnair W, Robinson MD. Doublet identification in single-cell sequencing data using scDblFinder. F1000Res. 2021;10:979.

29. Korsunsky I, Millard N, Fan J, Slowikowski K, Zhang F, Wei K, et al. Fast, sensitive and accurate integration of single-cell data with Harmony. Nat Methods. 2019;16(12):1289–96.
30. Collin J, Hasoon MSR, Zerti D, Hammadi S, Dorgau B, Clarke L, et al. Single-cell RNA sequencing reveals transcriptional changes of human choroidal and retinal pigment epithelium cells during fetal development, in healthy adult and intermediate age-related macular degeneration. Hum Mol Genet. 2023;32(10):1698–710.
31. Zauhar R, Biber J, Jabri Y, Kim M, Hu J, Kaplan L, et al. As in Real Estate, Location Matters: Cellular Expression of Complement Varies Between Macular and Peripheral Regions of the Retina and Supporting Tissues. Front Immunol. 2022;13:895519.
32. Butler A, Hoffman P, Smibert P, Papalexi E, Satija R. Integrating single-cell transcriptomic data across different conditions, technologies, and species. Nat Biotechnol. 2018;36(5):411–20.
33. Subramanian A, Tamayo P, Mootha VK, Mukherjee S, Ebert BL, Gillette MA, et al. Gene set enrichment analysis: a knowledge-based approach for interpreting genome-wide expression profiles. Proc Natl Acad Sci U S A. 2005;102(43):15545–50.
34. Jin S, Plikus MV, Nie Q. CellChat for systematic analysis of cell-cell communication from single-cell transcriptomics. Nat Protoc. 2025;20(1):180–219.
35. Shao X, Wang Z, Wang K, Lu X, Zhang P, Guo R, et al. A Single-Cell Landscape of Human Liver Transplantation Reveals a Pathogenic Immune Niche Associated with Early Allograft Dysfunction. Engineering. 2024;36:193–208.
36. Browaeys R, Saelens W, Saeys Y. NicheNet: modeling intercellular communication by linking ligands to target genes. Nat Methods. 2020;17(2):159–62.
37. Morabito S, Reese F, Rahimzadeh N, Miyoshi E, Swarup V. hdWGCNA identifies co-expression networks in high-dimensional transcriptomics data. Cell Rep Methods. 2023;3(6):100498.
38. Langfelder P, Horvath S. WGCNA: an R package for weighted correlation network analysis. BMC Bioinformatics. 2008;9:559.
39. Andreatta M, Carmona SJ. UCell and pyUCell: single-cell gene signature scoring for R and Python. Bioinformatics. 2026;42(2).
40. Aibar S, González-Blas CB, Moerman T, Huynh-Thu VA, Imrichova H, Hulselmans G, et al. SCENIC: single-cell regulatory network inference and clustering. Nat Methods. 2017;14(11):1083–6.
41. Trapnell C, Cacchiarelli D, Grimsby J, Pokharel P, Li S, Morse M, et al. The dynamics and regulators of cell fate decisions are revealed by pseudotemporal ordering of single cells. Nat Biotechnol. 2014;32(4):381–6.
42. Qiu X, Mao Q, Tang Y, Wang L, Chawla R, Pliner HA, et al. Reversed graph embedding resolves complex single-cell trajectories. Nat Methods. 2017;14(10):979–82.
43. Natoli R, Jiao H, Barnett NL, Fernando N, Valter K, Provis JM, et al. A model of progressive photo-oxidative degeneration and inflammation in the pigmented C57BL/6J mouse retina. Exp Eye Res. 2016;147:114–27.
44. Long Y, Ang KS, Li M, Chong KLK, Sethi R, Zhong C, et al. Spatially informed clustering, integration, and deconvolution of spatial transcriptomics with GraphST. Nat Commun. 2023;14(1):1155.
45. Graw J, Neuhäuser-Klaus A, Klopp N, Selby PB, Löster J, Favor J. Genetic and allelic heterogeneity of Cryg mutations in eight distinct forms of dominant cataract in the mouse. Invest Ophthalmol Vis Sci. 2004;45(4):1202–13.
46. Macosko EZ, Basu A, Satija R, Nemesh J, Shekhar K, Goldman M, et al. Highly Parallel Genome-wide Expression Profiling of Individual Cells Using Nanoliter Droplets. Cell. 2015;161(5):1202–14.
47. Xu S, Hu E, Cai Y, Xie Z, Luo X, Zhan L, et al. Using clusterProfiler to characterize multiomics data. Nat Protoc. 2024;19(11):3292–320.
48. Betjes MG, Haks MC, Tuk CW, Beelen RH. Monoclonal antibody EBM11 (anti-CD68) discriminates between dendritic cells and macrophages after short-term culture. Immunobiology. 1991;183(1–2):79–87.
49. Voigt AP, Mulfaul K, Mullin NK, Flamme-Wiese MJ, Giacalone JC, Stone EM, et al. Single-cell transcriptomics of the human retinal pigment epithelium and choroid in health and macular degeneration. Proc Natl Acad Sci U S A. 2019;116(48):24100–7.
50. Xiao SY, Lv YH, Ji YM, Dong Y, Liu MC, Li T, et al. The NLRP3 inflammasome: a pivotal orchestrator of multisystem diseases-from molecular mechanisms to therapeutic innovation. Mol Biol Rep. 2025;52(1):1026.
51. Forde H, Harper E, Rochfort KD, Wallace RG, Davenport C, Smith D, et al. TRAIL inhibits oxidative stress in human aortic endothelial cells exposed to pro-inflammatory stimuli. Physiol Rep. 2020;8(20):e14612.
52. Germano G, Frapolli R, Belgiovine C, Anselmo A, Pesce S, Liguori M, et al. Role of macrophage targeting in the antitumor activity of trabectedin. Cancer Cell. 2013;23(2):249–62.
53. Huang L, Ye L, Li R, Zhang S, Qu C, Li S, et al. Dynamic human retinal pigment epithelium (RPE) and choroid architecture based on single-cell transcriptomic landscape analysis. Genes Dis. 2023;10(6):2540–56.
54. Fleckenstein M, Mitchell P, Freund KB, Sadda S, Holz FG, Brittain C, et al. The Progression of Geographic Atrophy Secondary to Age-Related Macular Degeneration. Ophthalmology. 2018;125(3):369–90.
55. Kauppinen A, Paterno JJ, Blasiak J, Salminen A, Kaarniranta K. Inflammation and its role in age-related macular degeneration. Cell Mol Life Sci. 2016;73(9):1765–86.
56. Borchert GA, Shamsnajafabadi H, Hu ML, De Silva SR, Downes SM, MacLaren RE, et al. The role of inflammation in age-related macular degeneration-therapeutic landscapes in geographic atrophy. Cells. 2023;12(16).
57. Wang K, Zheng M, Lester KL, Han Z. Light-induced Nrf2(-/-) mice as atrophic age-related macular degeneration model and treatment with nanoceria laden injectable hydrogel. Sci Rep. 2019;9(1):14573.
58. Cox K, Shi G, Read N, Patel MT, Ou K, Liu Z, et al. Age-Associated Decline in Autophagy Pathways in the Retinal Pigment Epithelium and Protective Effects of Topical Trehalose in Light-Induced Outer Retinal Degeneration in Mice. Aging Cell. 2025;24(7):e70081.
59. Wooff Y, Cioanca AV, Wills E, Chu-Tan JA, Sekar R, Natoli R. Short exposure to photo-oxidative damage triggers molecular signals indicative of early retinal degeneration. Front Immunol. 2023;14:1088654.
60. Ronning KE, Karlen SJ, Miller EB, Burns ME. Molecular profiling of resident and infiltrating mononuclear phagocytes during rapid adult retinal degeneration using single-cell RNA sequencing. Sci Rep. 2019;9(1):4858.
61. Lei S, Hu M, Wei Z. Single-cell sequencing reveals an important role of SPP1 and microglial activation in age-related macular degeneration. Front Cell Neurosci. 2023;17:1322451.
62. O'Koren EG, Yu C, Klingeborn M, Wong AYW, Prigge CL, Mathew R, et al. Microglial Function Is Distinct in Different Anatomical Locations during Retinal Homeostasis and Degeneration. Immunity. 2019;50(3):723–e377.
63. Voigt AP, Mullin NK, Mulfaul K, Lozano LP, Wiley LA, Flamme-Wiese MJ, et al. Choroidal endothelial and macrophage gene expression in atrophic and neovascular macular degeneration. Hum Mol Genet. 2022;31(14):2406–23.
64. Droho S, Thomson BR, Makinde HM, Cuda CM, Perlman H, Lavine JA. Ocular macrophage origin and heterogeneity during steady state and experimental choroidal neovascularization. J Neuroinflammation. 2020;17(1):341.
65. Kelly J, Ali Khan A, Yin J, Ferguson TA, Apte RS. Senescence regulates macrophage activation and angiogenic fate at sites of tissue injury in mice. J Clin Invest. 2007;117(11):3421–6.
66. Pan S, Tang H, Yao B, Tian G, Sun B, Hu Y, et al. Decoding the ontogeny of myeloid lineage diversity by cross-species and developmental analyses of hematopoietic progenitor atlases. Cell Rep. 2025;44(3):115406.
67. Du S, Nguyen KM, Ulezko Antonova A, Fachi JL, Rodrigues PF, Verdiani A, et al. Publisher Correction: Diversity and immune dynamics of choroid plexus macrophages are shaped by distinct developmental origins. Nat Neurosci. 2026;29(3):761.
68. Kinuthia UM, Wolf A, Langmann T. Microglia and Inflammatory Responses in Diabetic Retinopathy. Front Immunol. 2020;11:564077.
69. Xu J, Tu Y, Wang Y, Xu X, Sun X, Xie L, et al. Prodrug of epigallocatechin-3-gallate alleviates choroidal neovascularization via down-regulating HIF-1α/VEGF/VEGFR2 pathway and M1 type macrophage/microglia polarization. Biomed Pharmacother. 2020;121:109606.
70. Biesemeier A, Taubitz T, Julien S, Yoeruek E, Schraermeyer U. Choriocapillaris breakdown precedes retinal degeneration in age-related macular degeneration. Neurobiol Aging. 2014;35(11):2562–73.
71. Whitmore SS, Sohn EH, Chirco KR, Drack AV, Stone EM, Tucker BA, et al. Complement activation and choriocapillaris loss in early AMD: implications for pathophysiology and therapy. Prog Retin Eye Res. 2015;45:1–29.
72. Ren X, Manzanares LD, Piccolo EB, Urbanczyk JM, Sullivan DP, Yalom LK, et al. Macrophage-endothelial cell crosstalk orchestrates neutrophil recruitment in inflamed mucosa. J Clin Invest. 2023;133(15).
73. Thayaparan D, Emoto T, Khan AB, Besla R, Hamidzada H, El-Maklizi M, et al. Endothelial dysfunction drives atherosclerotic plaque macrophage-dependent abdominal aortic aneurysm formation. Nat Immunol. 2025;26(5):706–21.
74. Sheridan JP, Marsters SA, Pitti RM, Gurney A, Skubatch M, Baldwin D, et al. Control of TRAIL-induced apoptosis by a family of signaling and decoy receptors. Science. 1997;277(5327):818–21.
75. Ravi R, Bedi A. Sensitization of tumor cells to Apo2 ligand/TRAIL-induced apoptosis by inhibition of casein kinase II. Cancer Res. 2002;62(15):4180–5.
76. El Ghrably I, Powe DG, Orr G, Fischer D, McIntosh R, Dua HS, et al. Apoptosis in proliferative vitreoretinopathy. Invest Ophthalmol Vis Sci. 2004;45(5):1473–9.

77. Harper E, Rochfort KD, Forde H, Davenport C, Smith D, Cummins PM. TRAIL attenuates RANKL-mediated osteoblastic signalling in vascular cell monoculture and co-culture models. PLoS ONE. 2017;12(11):e0188192.
78. Davidovich P, Higgins CA, Najda Z, Longley DB, Martin SJ. cFLIP(L) acts as a suppressor of TRAIL- and Fas-initiated inflammation by inhibiting assembly of caspase-8/FADD/RIPK1 NF-κB-activating complexes. Cell Rep. 2023;42(12):113476.
79. Zhang H, Chen Y, Li Y, Chen C, Wang B, Yin F, et al. TNFSF10 drives hyperactive immune responses via NLRP3 inflammasome and endoplasmic reticulum stress in autoimmune and inflammatory diseases. J Adv Res. 2026.
80. Burgaletto C, Platania CBM, Di Benedetto G, Munafò A, Giurdanella G, Federico C, et al. Targeting the miRNA-155/TNFSF10 network restrains inflammatory response in the retina in a mouse model of Alzheimer's disease. Cell Death Dis. 2021;12(10):905.
81. Müller CW, Rey FA, Sodeoka M, Verdine GL, Harrison SC. Structure of the NF-kappa B p50 homodimer bound to DNA. Nature. 1995;373(6512):311–7.

Publisher's note